Advanced Functional Materials

ADVANCED FUNCTIONAL MATERIALS
www.afm-journal.de

RESEARCH ARTICLE OPEN ACCESS

Coherent Control of Nitrogen Nuclear Spins via the V_B^--Center in Hexagonal Boron Nitride

Adalbert Tibiássy[1,2] | Charlie J. Patrickson[3] | Thomas Poirier[4] | James H. Edgar[4] | Bruno Lopez-Rodriguez[5] | Viktor Ivády[1,2] | Isaac J. Luxmoore[3]

[1]Department of Physics of Complex Systems, Eötvös Loránd University, Budapest, Hungary | [2]MTA–ELTE Lendület "Momentum" NewQubit Research Group, Budapest, Hungary | [3]Department of Engineering, University of Exeter, Exeter, UK | [4]Tim Taylor Department of Chemical Engineering, Kansas State University, Manhattan, Kansas, USA | [5]Department of Imaging Physics (ImPhys), Faculty of Applied Sciences, Delft University of Technology, Delft, The Netherlands

Correspondence: Viktor Ivády (ivady.viktor@ttk.elte.hu) | Isaac J. Luxmoore (i.j.luxmoore@exeter.ac.uk)

Received: 7 October 2025 | **Revised:** 22 December 2025

Keywords: coherence protection | decoherence | quantum sensing | V_B^- center in hBN

ABSTRACT

Charged boron vacancies (V_B^-) in hexagonal boron nitride (hBN) have emerged as a promising platform for quantum nanoscale sensing and imaging. While these primarily involve electron spins, nuclear spins provide an additional resource for quantum operations. This work presents a comprehensive experimental and theoretical study of the properties and coherent control of the nearest-neighbor ^{15}N nuclear spins of V_B^--ensembles in isotope-enriched $h^{10}B^{15}N$. Multi-nuclear spin states are selectively addressed, enabled by the state-specific nuclear spin transitions arising from spin-state mixing. We perform Rabi driving between selected state pairs, define elementary quantum gates, and measure longer than 10 μs nuclear Rabi coherence times. We observe a two orders of magnitude nuclear g-factor enhancement that underpins fast nuclear spin gates. Accompanying numerical simulations provide a deep insight into the underlying mechanisms. These results establish the foundations for leveraging nuclear spins in V_B^- center-based quantum applications, particularly for extending coherence times and enhancing the sensitivity of 2D quantum sensing foils.

1 | Introduction

Spin defects in wide bandgap semiconductors have emerged as a promising platform for nanoscale quantum sensing, dominated by the nitrogen vacancy (NV) center in diamond [1, 2], thanks to its long coherence times [3] and efficient optical spin polarization at room temperature [1, 2]. NV centers can be applied in dense ensembles to reach pT/$\sqrt{\text{Hz}}$ level sensitivities [4, 5], or mounted individually in diamond tips to probe magnetism with nanoscale spatial resolution [6, 7]. There is growing interest in directly integrating quantum sensors [8] with the probed system to achieve higher spatial resolution. Examples include introducing spin defects in nanoscale particles to biological samples [9–11], and direct integration of the system of interest with a quantum sensing chip [12–14]. This is challenging with NV centers, as the diamond host is difficult to process, and the NV coherence time is substantially degraded when located close to the sample surface due to charge trapping effects. In contrast, with hBN, the defects remain effective when they are in 2–3 nm proximity of the material's surface [15]. Consequently, they can be in proximate contact or be embedded within the target system, and are inherently well-suited to heterogeneous integration thanks to well-developed pick and place fabrication methods. This approach has been applied to study magnetism in 2D [16–18]

and bulk [19, 20] magnetic materials, with ensembles of boron vacancy defects V_B^- in hBN flakes directly integrated with the target platforms.

The V_B^- has been thoroughly studied by experiments [21] and theory [22, 23], testifying the keen interest and potential of spin defects in 2D materials. Like the NV center in diamond, V_B^- is a radiative spin triplet system (total spin quantum number, S = 1). It has ground- and excited-state zero-field splitting of ∼3.5 GHz [21] and ∼2.1 GHz [24, 25], respectively. Spin initialization can be achieved through optical pumping. One important shortcoming of the V_B^- center, compared to the NV center in diamond, is its low intrinsic quantum efficiency [22], which prohibits single-defect measurements. This limitation may, however, be counterbalanced by the efficient creation of V_B^- centers by neutron irradiation, which may lead to high densities of V_B^- centers even in ultrathin hBN samples. [15] Room-temperature electron spin relaxation, T_1 and spin coherence, T_2, times are ∼ 20 μs [26] and ∼ 100 ns [27–31], respectively. Various dynamical decoupling schemes can effectively extend T_2 [28, 29, 32], and enhance sensing performance [29, 33, 34]. Consequently, the V_B^- center is an alternative to the NV center due to its potentially superior performance in near-surface sensing and imaging applications. [35]

Strong hyperfine coupling provides a mechanism to polarize and control the three nearest neighbor nitrogen nuclei via the V_B^- electron spin [36–41]. Optical pumping via spin mixing near the avoided crossings of the excited and ground states (ESLAC and GSLAC) has been shown to partially polarize the nitrogen nuclei [36, 38–40], while coherent control of the nuclear spins can be achieved using electron-nuclear double resonance (ENDOR) techniques [36, 38, 41].

In this article, we explore and demonstrate the coherent control of ^{15}N nitrogen nuclear spins adjacent to the V_B^- center in an isotopically enriched hBN crystal [42]. We perform an electron-nuclear double resonance study and selectively address the four nuclear spin states of the three identical spin-1/2 nitrogen nuclei. Theory predicts that this selective addressability arises from electron-nuclear hyperfine coupling, which induces state-dependent mixing of the two spin species. This mixing results in distinct shifts lifting the degeneracy of the transitions. Hyperfine mixing significantly enhances the nuclear g-factor, resulting in an increase of the Rabi frequency by approximately a factor of 164 compared to that of pure nuclear spin states. In addition, Rabi oscillation of the nuclear spin has a coherence time exceeding 10 μs, and there is an unexpected loss of nuclear polarization when pumping the defect optically. The narrow magnetic resonance line width, long coherence time, and fast nuclear spin control make nuclear spins adjacent to V_B^- centers a desirable platform for quantum applications, especially in the field of quantum sensing.

Before presenting our results, we briefly review the most relevant properties of the V_B^- center that provide the basis for our discussions. The V_B^- center is a planar defect in hBN with D_{3h} symmetry. The defect electronic states in the bandgap arise from in-plane nitrogen dangling bonds, which define the spin density (see Figure 1a), and from the out-of-plane p_z orbitals of the neighboring nitrogen atoms. The latter orbitals play an important role in forming the optically excited triplet state [22, 43]. Each lattice site in hBN contains a nuclear magnetic moment that interacts with the electron spin through dipole–dipole and Fermi contact hyperfine interaction terms obtained from the spin density distribution of the defect. In our experiments and simulations, we study boron-10 and nitrogen-15 isotope enriched $h^{10}B^{15}N$ crystals. Due to the localized nature of the defect orbitals and thus the spin density, see Figure 1, the V_B^- center couples most strongly to the three nearest-neighbor ^{15}N nuclear spins ($I = 1/2$). Indeed, the dynamics of the V_B^- electron spin cannot be considered separately from its first neighbor nuclear spins, and these four spins form an entangled core. [37, 44] The second and third-strongest hyperfine interactions are approximately one and two orders of magnitude smaller [22, 44], respectively, allowing us to investigate the properties of the electron spin and its three nearest-neighbor nuclei independently of the surrounding nuclear spin bath in first order.

Hyperfine interaction with the nearest neighbor ^{15}N spin is crucially important in our study, thus, we examine different terms of the coupling and their effect in the presence of an external magnetic field separately. In this study, we employ a constant B magnetic field parallel to the symmetry axis of the defect, which is also aligned with the preferential quantization axis of the defects set by the zero-field splitting interaction of the ground-state electron spin. The static Hamiltonian for the electron and the three ^{15}N nuclear spin can be written as,

$$\hat{H} = DS_z^2 + \gamma_e S_z B + \sum_{i=1}^{3} \left(\gamma_{^{15}N} I_{z,i} B + \mathbf{S} A_i \mathbf{I}_i \right) \quad (1)$$

where γ_e and $\gamma_{^{15}N}$ are the gyromagnetic ratios of the electron and the nuclear spins, $\mathbf{S}$ and $\mathbf{I}_i$ are the electron and nuclear spin operator vectors, respectively, and D is the parallel zero-field splitting parameter. The transverse zero field splitting parameter E is neglected in our study, since we focus predominantly on the 150–250 mT magnetic field range, where E has a negligible effect. Finally, A_i are the hyperfine coupling tensors of the first neighbor nuclear spins, for which we initially use published theoretical tensors [22] and later scale to perfectly match our experimental nuclear magnetic resonance spectra. Throughout this article, we use a common Cartesian frame to express the hyperfine tensors A_i, in which the z axis is perpendicular to the plane, and the x and y axes lie in the plane, with the x axis passing through one of the first-neighbor nitrogen atoms. In this frame, $A_{zz} = A_{\parallel}$ accounts for the diagonal (secular) term of the Hamiltonian, while A_{xx}, A_{yy}, and $A_{yx} = A_{xy}$ account for the mixing of the electron and nuclear spins. It is worth noting that the rotationally invariant mixing term appearing in perturbation theory is given by $A_{\perp} = \sqrt{\left(A_{xx} + A_{yy}\right)^2 + 4A_{xy}^2}$.

Magnetic field dependence of the spin eigenstates of the four-spin system is depicted in Figure 1b. The eigenstates are separated into three branches according to the electron spin m_S quantum numbers, except at the ground state level avoided crossing (GSLAC) where the $m_S = 0$ and the $m_S = -1$ states are heavily mixed by the hyperfine coupling of the first neighbor nuclei ^{15}N, see Figure 1b. Away from the GSLAC, the secular hyperfine couplings A_{zz} of the three first neighbor spin-1/2 ^{15}N nuclear spins give rise to a characteristic four-peak hyperfine structure [39] of

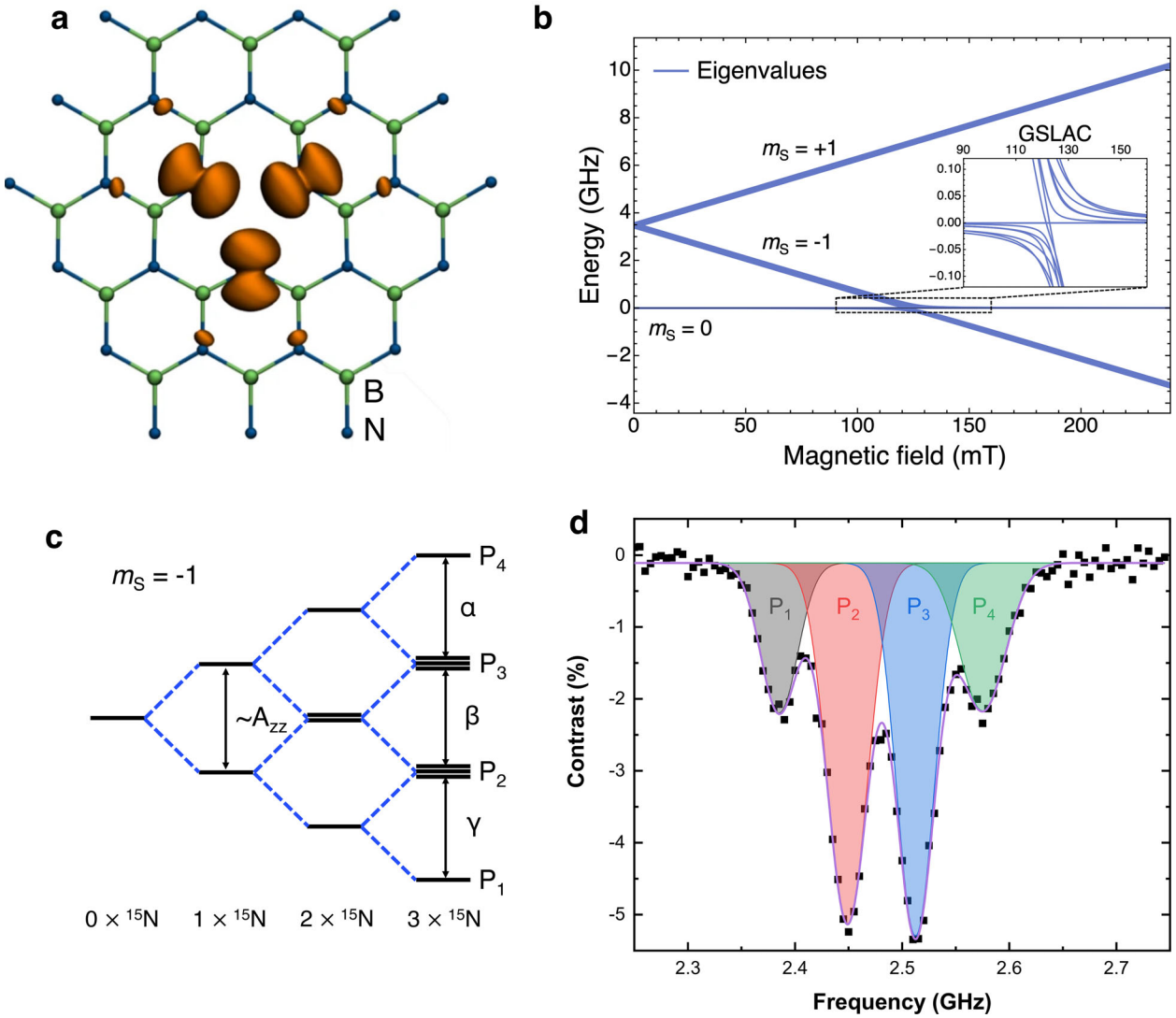

FIGURE 1 | Configuration and fine electronic structure of the V_B^- center in $h^{10}B^{15}N$. (a) Structure and electron spin density (dark orange lobes) of the V_B^--center in hBN. Green and deep blue spheres depict nitrogen and boron atomic positions. (b) Magnetic field dependence of the spin energy levels. The inset depicts the energy levels at the ground state level avoided crossing (GSLAC) region of strong electron-nuclear spin mixing. (c) Emergence of the hyperfine structure in the $m_S = -1$ branch in $h^{10}B^{15}N$ away from the GSLAC in secular approximation. (d) ODMR spectra of the V_B^- center in $h^{10}B^{15}N$ at 212 mT fitted with a sum of four Gaussian curves.

the $m_S = \pm 1$ branches of the V_B^- center with 1-3-3-1 degeneracies in $h^{10}B^{15}N$, see Figure 1c. Figure 1c details how the degenerate states are formed, assuming each added nuclear spin splits the energy levels equally (see the dashed blue lines), corresponding to the secular A_{zz} component for each nucleus. Since the system exhibits a 120° rotation symmetry, all first neighbor ^{15}N A_{zz} components are the same.

2 | Results

First, we carry out optically detected magnetic resonance (ODMR) on the ensemble of V_B^- in $h^{10}B^{15}N$ by driving the $m_S = 0 \leftrightarrow m_S = -1$ transition at 212 mT. A characteristic four-peak hyperfine structure is observed, see Figure 1d, where the peaks are labeled as P_1-P_4 in order of increasing energy for the $m_S = -1$ state, and correspond to $m_{J_z} = \{+3/2, +1/2, -1/2, -3/2\}$ quantum numbers of $J_z = \sum_i I_{z,i}$ in the secular approximation, i.e., when only the diagonal elements of the spin Hamiltonian are considered. When the nuclear spins are not polarized, i.e., all states are occupied with equal probability, the areas under the ODMR peaks P_1-P_4 are proportional to the 1-3-3-1 degeneracy of the hyperfine levels.

To selectively address the nuclear spin states of the V_B^- center, we carry out pulsed ENDOR studies on our isotope-enriched sample, see Methods for further details. We first initialize the electron spin predominantly in the $m_S = 0$ subspace by a blue (488 nm) laser pulse and apply a microwave (MW) π-pulse with frequency ω_i to selectively populate one of the peaks P_1-P_4. This transition is nuclear spin state selective (CNOT gate). Assuming a uniform population of the nuclear spin states, the population transferred to the $m_S = -1$ state after the MW pulse is proportional to the number of the hyperfine levels involved in the transition, see Figure 1c. After some population is transferred to the $m_S = -1$ branch, a radiofrequency (RF) pulse with a varying frequency

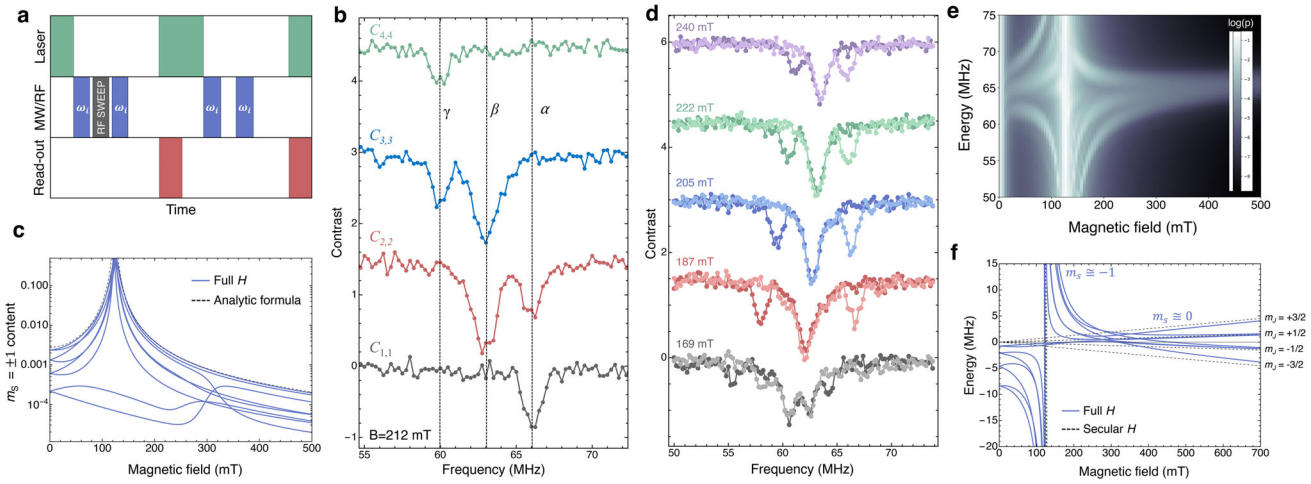

FIGURE 2 | Electron nuclear double resonance of first neighbor nitrogen nuclear spins. (a) Pulse sequence of nuclear spin state control. Sage green, slate blue, and gray rectangles represent laser, microwave (MW), and radio frequency (RF) pulses, while the terracotta pink rectangles represent the period of photon collection. The pulse durations are not to scale. (b) Electron nuclear double resonance (ENDOR) spectra of the V_B^- center in $h^{10}B^{15}N$. Green, blue, terracotta, and gray curves show the ENDOR contrast $C_{i,i}$ obtained by initializing and measuring the same P_i hyperfine sublevel, see Figure 1d. Here, an external magnetic field of 212 mT is used in the measurements. (c) The amount of mixing of the electron spin $m_S = \pm 1$ states with the dominantly $m_S = 0$ state. The value 0.01 means 1% mixing. Blue lines depict the mixing of the hyperfine resolved states obtained by diagonalizing the full Hamiltonian, while the dashed gray line depicts the result of a simple analytical formula assuming only electron spin state splitting and hyperfine mixing terms of strength $A_\perp$, see text. (d) Magnetic field dependence of the ENDOR resonance peaks for $C_{2,2}$ (light) and $C_{3,3}$ (dark). The spectra in (b) and (d) are offset for clarity. The actual ENDOR contrast falls in the range of 0.6–1.5%. (e) simulated wide field magnetic dependence of the ENDOR resonance peaks. The density map p is obtained by summing up all $C_{i,i}$ curves at all magnetic field values. (f) Close-up view of the magnetic field dependence of the energy levels of the $m_S = 0$ branch.

is applied to drive resonant transitions between the populated and unpopulated hyperfine states. The duration of the pulse is set to approximately perform a π-pulse between the hyperfine states when the RF drive is resonant with the transition, which we do by performing a Rabi-oscillation and selecting the duration corresponding to the first minima in the contrast. Finally, another MW π-pulse with frequency ω_j is applied to selectively test the population of peak P_j. After performing this pulse sequence, the electron spin population carries information on the success of the nuclear spin transition, which is then read out via the photoluminescence intensity at the beginning of the next laser pulse. The sequence is repeated without applying the RF pulse for better contrast. Finally, the pulsed ENDOR signal is obtained as

$$C_{i,j} = \frac{I^{i,j}_{\text{on}} - I^{i,j}_{\text{off}}}{I^{i,j}_{\text{off}}} \tag{2}$$

where $I^{i,j}_{\text{on (off)}}$ is the PL intensity detected while addressing peaks P_i and P_j with MW transition frequencies ω_i and ω_j for RF drive on (off).

Sample ENDOR spectra are depicted in Figure 2b. In each measurement, we populate peaks P_1, P_2, P_3, or P_4 with the first MW pulse and examine the population of the same peaks after the RF pulse ($C_{i,i}$ signals), see Figure 2a. Dips in the contrast indicate successful nuclear spin population transfer from the initial hyperfine state i to other hyperfine states with $\Delta m_{J,z} \simeq \pm 1$. As can be seen in Figure 2b, starting from the lowest energy P_1 state, there is only one nuclear resonance transition. For the case of middle P_2 and P_3 states, there are two possible transition frequencies, while for the P_4 state, again, a single transition energy is revealed. Altogether, three distinct transition energies labelled α, β, and γ are observed, see Figures 1c and 2b. Our protocol thus enables selective initialization of the 4-spin system in all the hyperfine states in the $m_S = -1$ branch.

Strikingly, the α, β, and γ nuclear spin state transition energies exhibit notable differences. Considering only the secular, diagonal terms of the system's spin Hamiltonian, one would expect that these transition energies are equal, see Figure 1c, since the A_{zz} component of the hyperfine tensors of the first-neighbor nitrogen atoms, causing the nuclear spin state splitting in first order, is identical due to the threefold rotational symmetry of the structure. However, the non-secular A_{xx}, A_{yy}, A_{xy}, and A_{yx} elements are significant, ranging from 20 to 92 MHz, which give rise to a mixing between the different m_S electron spin states. This mixing induces nuclear-spin-state-dependent shifts that, in turn, lead to measurable differences in the α, β, and γ transition energies. Moreover, since the degree of mixing varies across the investigated range of the external magnetic fields (Figure 2d), the α-γ transition energies consequently exhibit magnetic-field dependence. A comprehensive discussion and a perturbation-theory analysis of the mixing and the resulting energy shifts are provided in Note S1 and S2.

To test our theory, we perform pulsed ENDOR measurements at various magnetic field values as depicted in Figure 2d. The position of the nuclear resonance dips shows considerable magnetic field dependence in the examined 169–240 mT magnetic field interval, in agreement with the theoretical expectations. Closer to the GSLAC, we observe not only the shift of the α-γ transition energies, but also the splitting of the β transition.

The measurement in Figure 2d enables us to determine the hyperfine coupling of the first-neighbor nitrogen atoms with high accuracy. Utilizing exact diagonalization of the spin Hamiltonian and the method detailed in the Note S3, we fit the theoretical transition energies to the experimental results in the 187–240 mT magnetic field range. To obtain a good fit, a constant 0.947 isotropic scaling of the theoretical ^{15}N hyperfine tensors [22] was required. Thus, the secular and the mixing hyperfine tensor terms are $A_{zz} = A_{\parallel} = -63.7$ MHz and $A_{\perp} = 190.2$ MHz, respectively. In Figure 2 and in the rest of this study, we use the fitted hyperfine tensors.

Using accurate hyperfine values in our numerical simulations, we further extend the investigated magnetic field interval to 0–500 mT, see also Note S4. A density map of the population transfer summed up for all possible transitions is depicted in Figure 2e. Close to the GSLAC, in the 100–150 mT region, the deviations in the transition energies α, β, and γ become significant and reach the 10 MHz range. Interestingly, the characteristic three-peak transition energy spectrum is also resolved on the low-field side of the GSLAC, in the 10–100 mT interval, indicating that our ENDOR protocol can be applied at these magnetic fields as well, see also Note S5.

We also theoretically investigate the possibility of selectively driving the nuclear spin state at high magnetic fields. This requires that the differences between the α-β and β-γ transition energies exceed the width of the ENDOR lines. Both the splitting and the linewidth depend on the magnetic field through the degree of state mixing between the electron spin and the nuclear spins. Describing the splitting requires at least fourth-order perturbation theory, and thus the splitting scales as $\sim B^{-4}$, while the RF/MW broadening of the ENDOR lines is proportional to the g-factor enhancement, which scales as $\sim B^{-1}$ at high magnetic fields ($B \gg D/g_e\mu_B$). Due to this magnetic-field dependence, power broadening will exceed the splitting of the transition lines at some critical magnetic field, which will then merge into a single transition.

Under the conditions used in our experiments, we estimate that the loss of nuclear-spin-state selectivity due to the merging of the lines occurs around 0.6 T. However, with lower-power RF/MW driving, the nuclear spin states may remain separable even above 1 T, where the electron spin coherence time is significantly enhanced [30,31]. See Note S6 for further details.

Note that the splitting of the hyperfine states happens not only in the $m_S = \pm 1$ branches but also in $m_S = 0$ branch due to the mixing of the states. As can be seen in Figure 2f, the hyperfine splitting of the predominantly $m_S = 0$ states ranges between 2 and 20 MHz in the magnetic field interval of 0–500 mT. Therefore, nuclear spin state control is also possible in this RF frequency range in the $m_S = 0$ branch. The nuclear spin eigenstates in this branch are distinct from the I_z eigenbases since the splitting merely originates from the mixing of the nuclear spin states caused by the $A_{\perp}$ hyperfine term. Consequently, these states exhibit a highly irregular magnetic field dependence in the 0–500 mT interval, see Figure 2f.

Next, we study the Rabi drive of selected multi-nuclear spin state [36, 38] transitions α, β, and γ. For this study, we set the external magnetic field to 212 mT and employ the pulse sequence depicted in Figure 3a, where the width of the RF pulse is swept. With this ENDOR sequence, the contrast is approximately twice that of the standard sequence shown in Figure 2a. This enhancement arises because the sequence probes the population difference between two hyperfine states selected by the microwave pulses. When the RF field is resonant with a transition between these states, the population of one state increases while that of the other decreases, producing a differential signal. By contrast, the standard ENDOR sequence measures only the decrease in population of a single probed state, and therefore yields a smaller contrast (see also Note S7). An example of the Rabi oscillation between hyperfine sublevels P_3 and P_4 (transition γ) is depicted in Figure 3b. The power dependence of the Rabi frequency, studied on the Fourier spectrum of the nuclear spin oscillation, is shown in Figure 3c. We observe a single Fourier peak whose position linearly depends on the amplitude of the RF drive in accordance with the expectations. Next, we consider Rabi oscillation between hyperfine peaks P_2 and P_3, both of which are threefold degenerate in secular approximation, but possess unresolvable fine structure at 212 mT. As seen in Figure 3e,f, the dominant Rabi oscillation is perturbed by the other lower frequency oscillations that we attribute to the lifted degeneracy of the three states forming peaks P_2 and P_3. The fine structure of the peaks and the varying transition dipole moments of the nuclear spin state transition are depicted in Figure S1.

Next, we examine the dominant frequency of the Rabi oscillations. Setting the magnetic field to $B_z = 212$ mT, we drive both the electron spin state transitions between the $m_S = 0$ and $m_S = -1$ states, as well as the β and γ nuclear spin state transitions. Assuming that the MW and RF power are identical, the ratio of the Ω_e electron spin Rabi frequency and the Ω_α nuclear spin Rabi frequency is measured to be $\chi_{\text{effective}} = \Omega_e/\Omega_\alpha \sim 56$. These values are considerably smaller than the theoretical values for an isolated ^{15}N nuclear isotope, which is $\chi_{\text{isolated}} = \Omega_e/\Omega_{^{15}\text{N}} = 9180$. Consequently, the Rabi frequency of the first neighbor nuclear spin states of the V_B^- center in $h^{10}B^{15}N$ is enhanced compared to an isolated ^{15}N nuclear spin by a factor of $\chi_{\text{isolated}}/\chi_{\text{experiment}} = g^{\text{eff}}_{^{15}\text{N}}/g_{^{15}\text{N}} \approx 164$, which is in the same order as the observations of Ref. [38]. The enhancement of the nuclear g-factors is due to the non-negligible mixing of the electron and nuclear spin states in the presence of a strong hyperfine interaction. Due to the large gyromagnetic ratio of the electron spin compared to the ^{15}N nucleus, even a small mixing, see Figure 2c, can give rise to a large increase in the strength of the effective Zeeman interaction term. To quantify this, we derive the enhancement factor in the coupled basis of the three nitrogen ^{15}N nuclear spins, opposed to Ref. [38] where the nuclear spins are treated independently, and obtain the following formula for the largest enhancement factors for $P_2 \leftrightarrow P_3$ and $P_{1(3)} \leftrightarrow P_{2(4)}$ transitions,

$$\gamma \approx \frac{\xi}{3} \frac{g_e\mu_B}{g_{^{15}\text{N}}\mu_N} \frac{\left|A^{(1)}_{xx} + A^{(2)}_{xx} + A^{(3)}_{xx}\right|}{|D - g_e\mu_B B_z|} \tag{3}$$

where $A^{(i)}_{xx}$ is the xx element of the hyperfine tensor of nuclei i, D is the zero field splitting, B_z is the external magnetic field, and ξ takes the value of 2 and $\sqrt{3}$ for the $+1/2 \leftrightarrow -1/2$ ($P_2 \leftrightarrow P_3$) and the $\pm 1/2 \leftrightarrow \pm 3/2$ ($P_1 \leftrightarrow P_2$ and $P_3 \leftrightarrow P_4$) transitions in the quartet subspace of the coupled basis, see Note S8 for more details.

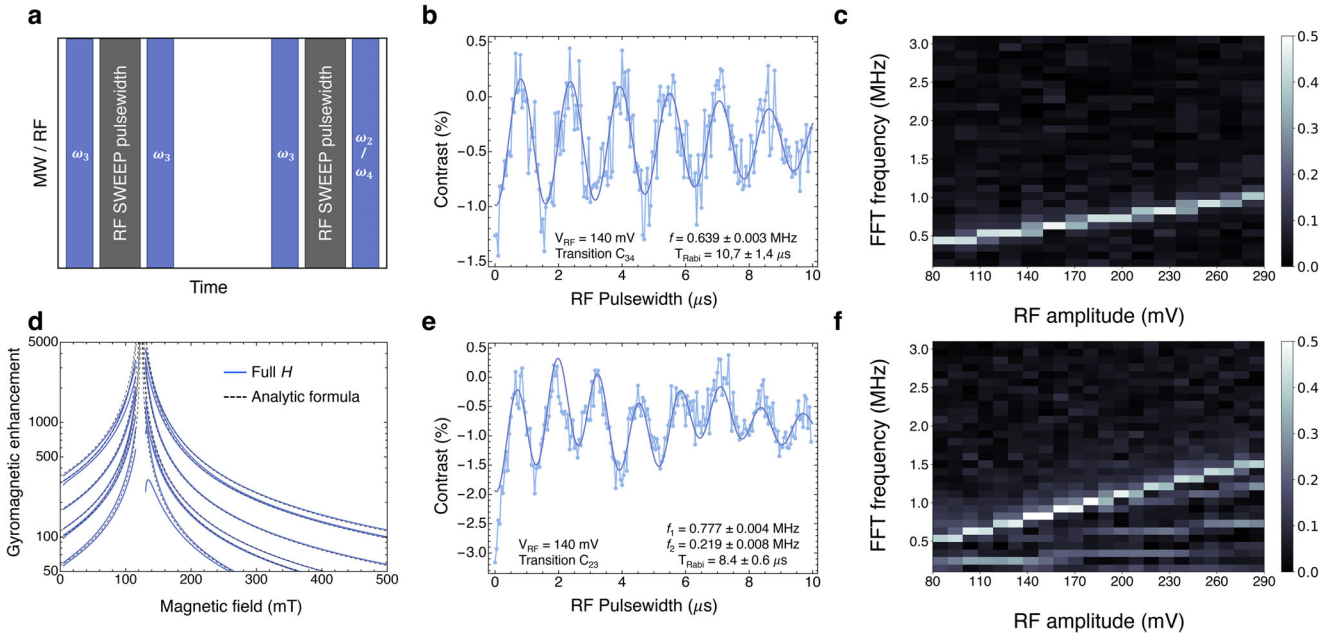

FIGURE 3 | Rabi drive of nitrogen nuclear spin states. (a) Differential ENDOR pulse sequence used for detecting the nuclear Rabi oscillation (b) Measured Rabi oscillation between hyperfine states P_3 and P_4. (c) Fourier amplitude map (gray scale) as a function of RF drive amplitude. The frequency of the Rabi oscillation varies linearly with the RF amplitude. (d) Computed nuclear g-factor enhancement resulting from the mixing of the electron and nuclear spin states. (e) Rabi oscillation between hyperfine peaks P_2 and P_3, and (f) the corresponding Fourier map. For the $P_2 \leftrightarrow P_3$ transition, the Rabi oscillation modulates due to the underlying structure of peaks P_2 and P_3 unresolved in our ENDOR spectra at the same B-field (212 mT).

The latter factor originates directly from the $\left\langle +1/2 \left| S_+^{(3/2)} \right| -1/2 \right\rangle$ and $\left\langle \pm 1/2 \left| S_+^{(3/2)} \right| \pm 3/2 \right\rangle$ matrix element of the ladder operator of the quartet spin. From our theory, we obtain that the frequency of the Rabi nutation between peaks $P_2 \leftrightarrow P_3$ is faster by a factor of $\eta = 2/\sqrt{3} = 1.154$ than the frequency of the Rabi nutation between the $P_1 \leftrightarrow P_2$ and $P_3 \leftrightarrow P_4$ peaks at the same RF power. This ratio is close to the experimentally measured ratio of 1.216 obtained from the measured nutation frequencies of $f_1 =$ 0.777 MHz for transition C_{23} in Figures 3d and $f = 0.639$ MHz for transition C_{34} in Figure 3b. Altogether, we identify ten nuclear spin state transitions with $\gamma > 1$, see Figure 3d and Note S8. At 212 mT, the theoretical g-factor enhancement is 416, which is in the same order of magnitude as the experimental value of ∼ 164, but a factor of 2.5 larger, presumably due to the uncertainty in the MW and RF power delivered to the sample and neglecting the other nuclear spins.

From a damped exponential fit to the data in Figure 3b, the Rabi coherence time is $T_{Rabi} \approx 12$ μs and trends downward with increasing RF drive amplitude. (see Note S9). This indicates the order of the T_2^* for the nuclear spin states in the weak drive limit ($T_{\mathrm{Rabi}} \approx T_2^*$) and is approximately two orders of magnitude longer than the T_2 coherence time of the electron spin.

Finally, we study the lifetime of the nuclear spin population under continuous optical drive. The pulse sequence used in the measurements is detailed in Figure 4a. For this measurement, we set the magnetic field to 212 mT. After populating a selected nuclear spin state with a MW and a subsequent RF pulse, we apply a laser pulse to repump the electron spin. The relative occupation of the nuclear spin states is then measured by sweeping the frequency of the microwave readout pulse for different repump pulsewidth t.

The nuclear spin polarization is calculated from the electron spin resonance spectra by fitting a sum of four Gaussian functions. The area of the four Gaussians, δ_{m_I} are used to estimate the nuclear polarization as:

$$\mathcal{P} = \left(\sum_{m_I} m_I \delta_{m_I} \right) / \left(\frac{3}{2} \sum_{m_I} \delta_{m_I} \right) \tag{4}$$

As can be seen in Figure 4b,c, after polarizing the nuclear spin system into the $m_I = -1/2$ sublevel, $\mathcal{P} = -0.27$, we observe a fast depolarization of the nuclear spin when the repump laser pulse is inserted. The optical cycling of the V_B^- center completely thermalizes the nuclear spin within 1 μs. Apparently, this timescale is shorter than the measured order of 10 μs nuclear spin Rabi T_2^* coherence time and much shorter than the expected T_1 time of the nuclear spins in the ground state.

Since the observed nuclear spin relaxation is a consequence of optical pumping, it can be attributed either to the spin and orbital momentum carrying optical excited $^3E''$ state or to the orbital momentum carrying $^1E'$ shelving state. The latter state may interact with the nuclear spins with the orbital hyperfine coupling enabled by the non-zero orbital and magnetic moment of the $^1E'$ state. On the other hand, the effective angular and, thus, the magnetic moment of the metastable state can be quenched substantially compared to a free-standing atom. For the excited state of the NV center in diamond, the effective l quantum number of L^2 operator is measured to be < 0.1 [2]. We assume the quenching to be in a similar order for the V_B^- center. Consequently, orbital hyperfine coupling is at least an order of magnitude smaller than the electron spin hyperfine coupling

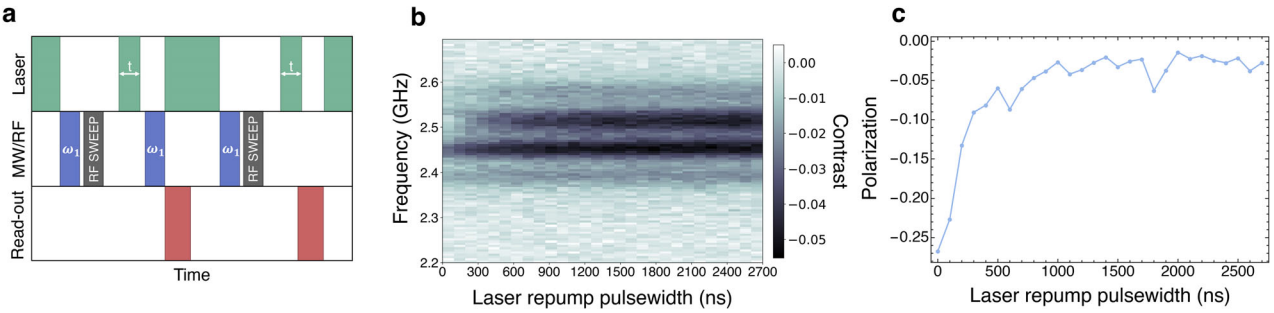

FIGURE 4 | Loss of nuclear spin polarization under optical pumping. (a) Pulse sequence used to study the repump laser duration dependence of the nuclear polarization. (b) ODMR map at $B = 212$ mT after employing a repump laser of varying duration. The maximal ODMR contrast in our measurements is ≈5%. (c) Polarization of the ^{15}N nuclear spin state as a function of the duration of the repump laser, see Figure 2a.

in the ground state. Since the stronger electron spin hyperfine coupling gives rise to slower nuclear spin relaxation in the ground state, we exclude orbital hyperfine coupling, and this way the ^{1}E′ state is the main cause of the optical pumping-induced nuclear spin relaxation.

We thus tentatively attribute the observed relaxation effects to the ^{3}E″ state. While fine details of this electronic state are still not well understood, from the preliminary studies [22, 43], we know that this state goes through significant Jahn–Teller distortion. Such a distortion does not imply a significant change in the hyperfine coupling [36], however, it may lead to new electron spin relaxation pathways through dynamical processes arising when transitions between the Jahn–Teller minima are enabled by temperature, which can shorten the lifetime of the electron spin. It is plausible that the electron spin states' fast relaxation can affect the nuclear spin through the spin state mixing caused by the hyperfine coupling.

3 | Discussion

Our results demonstrate that the three nearest-neighbor ^{15}N nuclear spins of the V_B^- center in isotope-enriched hBN are not merely a decoherence source, but instead provide a controllable quantum resource. By exploiting hyperfine-mediated mixing between electron and nuclear spin states, we selectively address multi-nuclear configurations and coherently manipulate specific state pairs with well-defined Rabi oscillations. The observed enhancement of the nuclear g-factor by more than two orders of magnitude compared to isolated ^{15}N nuclei enables rapid driving of the nuclear spin. Furthermore, the Rabi coherence times are one to two orders of magnitude longer than the electron spin T_2, underscoring the potential of nuclear spins mitigating decoherence in hBN-based quantum devices.

The fast control, long coherence times, and spectral selectivity of the strongly coupled nuclear spins provide a foundation for nuclear-assisted dynamics, quantum memories, and enhanced sensitivity in quantum sensing foils. The inherent 2D nature of hBN and stability of the V_B^- center in few-layer samples [46] facilitates direct integration with van der Waals heterostructures, opening new avenues for nanoscale quantum technologies for sensing [35].

4 | Methods

4.1 | Sample and Device Fabrication

Isotopically enriched h^{10}B^{15}N crystal flakes are grown by the atmospheric pressure high temperature (APHT) method, previously described in detail [42, 47, 48]. Briefly, the process starts by mixing high-purity 99.2% enriched boron-10 with nickel and chromium with mass ratios of 3.72:48.14:48.14, respectively. The mixture is then heated at 200°C/h under 97% enriched nitrogen-15 and hydrogen gas at pressures of 787 and 60 torr, respectively, to 1550°C, to produce a homogeneous molten solution. After 24 h, the solution is slowly cooled at 1°C/h, to 1500°C, then at 50°C/h to 1350°C, and 100°C/h to room temperature. The h^{10}B^{15}N solubility is decreased as the temperature is reduced, causing crystals to precipitate on the surface of the metal. The h^{10}B^{15}N flakes are exfoliated from the metal with thermal release tape. The free-standing h^{10}B^{15}N crystalline flakes are typically greater than 20 μm thick.

Thin flakes are tape-exfoliated and dry-transferred on top of a NbTiN/Cr/Au (100/5/200 nm) coplanar waveguide (CPW) on a sapphire substrate. The NbTiN layer was included for superconducting experiments, not reported here. After transfer to the CPW sample, the hBN was implanted with 2 keV He ions at a dose of 1×10^{14} cm^{-2} to induce the V_B^- ensemble.

4.2 | Experimental Setup

The experiments were performed under ambient conditions in a home-built scanning confocal microscope. A 488 nm diode laser is focused onto the sample using a high numerical aperture objective lens (NA = 0.8) and is modulated by an acousto-optic modulator. The boron vacancy photoluminescence is collected with the same objective, filtered by a 750 nm long pass filter (Thorlabs FELH0750) and coupled, via a multi-mode fiber to a single photon avalanche diode. The photon counts were recorded with time tagging electronics (Swabian Time Tagger 20). The microwave excitation was applied via the coplanar waveguide. The MW (electron) and RF (nuclear) pulses were generated by two independent channels of an arbitrary waveform generator (Keysight M8195A), amplified (Agilent 83017a for MW and Mini-Circuits TVA-R5-13 for RF), and then combined with a

power combiner (Mini-Circuits ZX10R-2-183-S+). The optical and microwave pulses and PL readout were synchronised using a pulse-pattern generator (Swabian Pulse Streamer 8). A permanent magnet is mounted below the sample on an XYZ-translation stage. The magnet's XY-position is adjusted to align the magnetic field parallel to the hBN hexagonal axis by maximizing the electron Rabi coherence time (see Note S10). All experiments are performed under ambient conditions.

4.3 | Numerical Simulations

For the theoretical part of this study, two main approaches were employed. The dynamics of the closed spin system were investigated through numerical simulations, with the governing equations implemented in C++. The system's time evolution was computed by solving the Liouville–von Neumann equation for the density operator, using a fourth-order Runge–Kutta integration scheme. The total simulated time was set to 600 ns, with a time step of 0.000005 ns.

The system was initialized in different quantum states to analyze nuclear spin transitions. Specifically, the density operator of the electronic spin was initially set to thermal equilibrium, while decoherence effects were neglected. Since the nuclear spin subsystem has a total of eight possible configurations, configurations with the same number of specific spin states were averaged to reduce computational complexity. The hyperfine interaction parameters used in the numerical simulations were obtained from ab initio calculations [22].

Transition matrix elements and fitted hyperfine values were computed using Mathematica. The Hamiltonian of the closed four-spin system was decomposed into two distinct components: the diagonalized Hamiltonian and the off-diagonal elements. The diagonalization was performed exactly, without any approximations. Transition matrix elements were then calculated for each pair of states.

Author Contributions

I.L. conceived and performed the spin-optical experiments with C.P. The CPW samples were designed by C.P. and fabricated by B.L. hBN flakes were synthesized by T.P. and J.E. A.T. and V.I. carried out the theoretical study and the computer simulations. The paper was written by V.I., A.T., and I.L. with inputs from all authors. The work was supervised by I.L. and V.I.

Acknowledgments

We thank Iman Esmaeil Zadeh for useful discussions and guidance in device fabrication. This research was supported by the National Research, Development, and Innovation Office of Hungary within the Quantum Information National Laboratory of Hungary (Grant No. 2022-2.1.1-NL-2022-00004) and grant FK 145395. We acknowledge the support of the European Union under Horizon Europe for the QRC-4-ESP project (Grant Agreement 101129663) and the QUEST project (Grant Agreement 101156088). The computations were enabled by resources provided by the National Academic Infrastructure for Supercomputing in Sweden (NAISS) and the Swedish National Infrastructure for Computing (SNIC) at NSC, partially funded by the Swedish Research Council through grant agreement no. 2022-06725 and no. 2018-05973. Support for the hexagonal boron nitride crystal growth was provided by the National Science Foundation, award number 2413808.

Conflicts of Interest

The authors declare no conflict of interest.

Data Availability Statement

The main data supporting the findings of this study are available within the paper and its Supplementary Information. Further numerical data are available from the authors upon reasonable request.

References

1. A. Gruber, A. Drabenstedt, C. Tietz, L. Fleury, J. Wrachtrup, and C. V. Borczyskowski, "Scanning Confocal Optical Microscopy and Magnetic Resonance on Single Defect Centers," *Science* 276, no. 5321: 2012–2014, https://doi.org/10.1126/science.276.5321.2012, http://www.sciencemag.org/cgi/content/abstract/276/5321/2012.

2. M. W. Doherty, N. B. Manson, P. Delaney, F. Jelezko, J. Wrachtrup, and L. C. L. Hollenberg, "The Nitrogen-Vacancy Colour Centre in Diamond," *Physics Reports* 528, no. 1 (2013): 1–45, https://www.sciencedirect.com/science/article/abs/pii/S0370157313000562 .

3. G. Balasubramanian, P. Neumann, D. Twitchen, et al., "Ultralong Spin Coherence Time in Isotopically Engineered Diamond," *Nature Materials* 8, no. 5 (2009): 383–387, https://doi.org/10.1038/nmat2420.

4. I. Fescenko, A. Jarmola, I. Savukov, et al., "Diamond Magnetometer Enhanced by Ferrite Flux Concentrators," *Physical Review Research* 2 (2020): 023394, https://doi.org/10.1103/PhysRevResearch.2.023394.

5. Z. Wang, F. Kong, P. Zhao, et al., "Picotesla Magnetometry of Microwave Fields with Diamond Sensors," *Science Advances* 8, no. 32 (2022): eabq8158, https://doi.org/10.1126/sciadv.abq8158.

6. L. Rondin, J.-P. Tetienne, T. Hingant, J.-F. Roch, P. Maletinsky, and V. Jacques, "Magnetometry with Nitrogen-Vacancy Defects in diamond," *Reports on Progress in Physics* 77, no. 5 (2014): 056503, https://doi.org/10.1088/0034-4885/77/5/056503.

7. Y. Xu, W. Zhang, and C. Tian, "Recent Advances on Applications of NV–Magnetometry in Condensed Matter Physics," *Photonics Research* 11, no. 3 (2023): 393–412, https://doi.org/10.1364/PRJ.471266.

8. G. Balasubramanian, I. Y. Chan, R. Kolesov, et al., "Nanoscale Imaging Magnetometry with Diamond Spins Under Ambient Conditions," *Nature* 455 (2008): 648–651, https://doi.org/10.1038/nature07278.

9. R. Schirhagl, K. Chang, M. Loretz, and C. L. Degen, "Nitrogen-Vacancy Centers in Diamond: Nanoscale Sensors for Physics and Biology," *Annual Review of Physical Chemistry* 65, no. 1 (2013): 83–105, https://doi.org/10.1146/annurev-physchem-040513-103659.

10. Y. Wu and T. Weil, "Recent Developments of Nanodiamond Quantum Sensors for Biological Applications," *Advanced Science* 9, no. 19 (2022): 2200059, https://doi.org/10.1002/advs.202200059.

11. X. Wang, J. Xu, S. Ge, et al., "Recent Applications of Nanodiamond Quantum Biosensors: A Review," *APL Materials* 11, no. 9 (2023): 090603, https://doi.org/10.1063/5.0170145.

12. K. D. Briegel, N. R. von Grafenstein, J. C. Draeger, P. Blümel, R. D. Allert, and D. B. Bucher, "Optical Widefield Nuclear Magnetic Resonance Microscopy," *Nature Communications* 16, no. 1 (2025): 1281, https://doi.org/10.1038/s41467-024-55003-5.

13. M. Cambria, S. Chand, C. M. Reiter, and S. Kolkowitz, "Scalable Parallel Measurement of Individual Nitrogen-Vacancy Centers," *Physical Review X* 15 (2025): 031015, https://doi.org/10.1103/jdzq-jbfz.

14. K.-H. Cheng, Z. Kazi, J. Rovny, et al., "Massively Multiplexed Nanoscale Magnetometry with Diamond Quantum Sensors," *Physical Review X* 15 (2025): 031014, https://doi.org/10.1103/t8fz-3tzs.

15. J. Fraunié, T. Clua-Provost, S. Roux, et al., "Charge State Tuning of Spin Defects in Hexagonal Boron Nitride," *Nano Letters* 25, no. 14 (2025): 5836–5842, https://doi.org/10.1021/acs.nanolett.5c00654.

16. M. Huang, J. Zhou, D. Chen, et al., "Wide Field Imaging of van der Waals Ferromagnet Fe3GeTe2 by Spin Defects in Hexagonal Boron Nitride," *Nature Communications* 13, no. 1 (2022): 5369, https://doi.org/10.1038/s41467-022-33016-2.

17. P. Kumar, F. Fabre, A. Durand, et al., "Magnetic Imaging with Spin Defects in Hexagonal Boron Nitride," *Physical Review Applied* 18 (2022): L061002, https://doi.org/10.1103/PhysRevApplied.18.L061002.

18. A. J. Healey, S. C. Scholten, T. Yang, et al., "Quantum Microscopy with van der Waals Heterostructures," *Nature Physics* 19, no. 1 (2023): 87–91, https://doi.org/10.1038/s41567-022-01815-5.

19. J. Zhou, H. Lu, D. Chen, et al., "Sensing Spin Wave Excitations by Spin Defects in Few-Layer-Thick Hexagonal Boron Nitride," *Science Advances* 10, no. 18 (2024): eadk8495, https://doi.org/10.1126/sciadv.adk8495.

20. H.-X. Zang, W. Jiang, N.-J. Guo, et al., "Detecting and Imaging of Magnons at Nanoscale with van der Waals Quantum Sensor," *Advanced Functional Materials* 35, no. 2: 2412166, https://doi.org/10.1002/adfm.202412166.

21. A. Gottscholl, M. Kianinia, V. Soltamov, et al., "Initialization and Read-Out of Intrinsic Spin Defects in a van der Waals Crystal at Room Temperature," *Nature Materials* 19, no. 5 (2020): 540–545, https://doi.org/10.1038/s41563-020-0619-6.

22. V. Ivády, G. Barcza, G. Thiering, et al., "Ab Initio Theory of the Negatively Charged Boron Vacancy Qubit in Hexagonal Boron Nitride," *npj Computational Materials* 6, no. 1 (2020): 41, https://doi.org/10.1038/s41524-020-0305-x.

23. A. Sajid, K. S. Thygesen, J. R. Reimers, and M. J. Ford, "Edge Effects on Optically Detected Magnetic Resonance of Vacancy Defects in Hexagonal Boron Nitride," *Communications Physics* 3, no. 1 (2020): 153, https://doi.org/10.1038/s42005-020-00416-z.

24. S. Baber, R. N. E. Malein, P. Khatri, et al., "Excited State Spectroscopy of Boron Vacancy Defects in Hexagonal Boron Nitride Using Time-Resolved Optically Detected Magnetic Resonance," *Nano Letters* 22, no. 1 (2021): 461–467, https://doi.org/10.1021/acs.nanolett.1c04366.

25. N. Mathur, A. Mukherjee, X. Gao, et al., "Excited-State Spin-Resonance Spectroscopy of V_B^- Defect Centers in Hexagonal Boron Nitride," *Nature Communications* 13, no. 1 (2022): 3233, https://doi.org/10.1038/s41467-022-30772-z.

26. A. Gottscholl, M. Diez, V. Soltamov, et al., "Room Temperature Coherent Control of Spin Defects in Hexagonal Boron Nitride," *Science Advances* 7, no. 14 (2021): eabf3630, https://doi.org/10.1126/sciadv.abf3630.

27. A. Haykal, R. Tanos, N. Minotto, et al., "Decoherence of VB^- Spin Defects in Monoisotopic Hexagonal Boron Nitride," *Nature Communications* 13, no. 1 (2022): 4347, https://doi.org/10.1038/s41467-022-31743-0 .

28. A. J. Ramsay, R. Hekmati, C. J. Patrickson, et al., "Coherence Protection of Spin Qubits in Hexagonal Boron Nitride," *Nature Communications* 14, no. 1 (2023): 461, https://doi.org/10.1038/s41467-023-36196-7.

29. R. Rizzato, M. Schalk, S. Mohr, et al., "Extending the Coherence of Spin Defects in hBN Enables Advanced Qubit Control and Quantum Sensing," *Nature Communications* 14, no. 1 (2023): 5089, https://doi.org/10.1038/s41467-023-40473-w.

30. A. Tárkányi and V. Ivády, "Understanding Decoherence of the Boron Vacancy Center in Hexagonal Boron Nitride," *Advanced Functional Materials* (2025): e11300, https://doi.org/10.1002/adfm.202511300 .

31. J. Lee, H. Kim, H. Park, and H. Seo, "Magnetic-Field Dependent VB^- Spin Decoherence in Hexagonal Boron Nitrides: A First-Principles Study," *Advanced Functional Materials* (2025): e11274, https://doi.org/10.1002/adfm.202511274.

32. R. Gong, G. He, X. Gao, et al., "Coherent Dynamics of Strongly Interacting Electronic Spin Defects in Hexagonal Boron Nitride," *Nature Communications* 14, no. 1 (2023): 3299, https://doi.org/10.1038/s41467-023-39115-y.

33. C. J. Patrickson, S. Baber, B. B. Gaál, A. J. Ramsay, and I. J. Luxmoore, "High Frequency Magnetometry with an Ensemble of Spin Qubits in Hexagonal Boron Nitride," *npj Quantum Information* 10, no. 1 (2024): 5, https://doi.org/10.1038/s41534-023-00796-4.

34. C. J. Patrickson, V. Haemmerli, S. Guo, A. J. Ramsay, and I. J. Luxmoore, "Microwave Quantum Heterodyne Sensing Using a Continuous Concatenated Dynamical Decoupling Protocol," *Nature Communications* 16, no. 1 (2025): 4380, https://doi.org/10.1038/s41467-025-59148-9.

35. D. M. Daly, N. R. Reed, S. J. DeVience, et al., "Prospects for Ultralow-Mass Nuclear Magnetic Resonance using Spin Defects in Hexagonal Boron Nitride," 2025, https://doi.org/10.48550/arXiv.2505.00383.

36. X. Gao, S. Vaidya, K. Li, et al., "Nuclear Spin Polarization and Control in Hexagonal Boron Nitride," *Nature Materials* 21, no. 1 (2022): 1024–1028, https://doi.org/10.1038/s41563-022-01329-8.

37. W. Liu, V. Ivády, Z.-P. Li, et al., "Coherent Dynamics of Multi-Spin V_B^- Center in Hexagonal Boron Nitride," *Nature Communications* 13, no. 1 (2022): 5713, https://doi.org/10.1038/s41467-022-33399-2.

38. R. Gong, X. Du, E. Janzen, et al., "Isotope Engineering for Spin Defects in van der Waals Materials," *Nature Communications* 15, no. 1 (2024): 104, https://doi.org/10.1038/s41467-023-44494-3.

39. T. Clua-Provost, A. Durand, Z. Mu, et al., "Isotopic Control of the Boron-Vacancy Spin Defect in Hexagonal Boron Nitride," *Physical Review Letters* 131, no. 12 (2023): 126901, https://doi.org/10.1103/physrevlett.131.126901.

40. S. Ru, Z. Jiang, H. Liang, et al., "Robust Nuclear Spin Polarization via Ground-State Level Anticrossing of Boron Vacancy Defects in Hexagonal Boron Nitride," *Physical Review Letters* 132 (2024): 266801, https://doi.org/10.1103/PhysRevLett.132.266801.

41. G. V. Mamin, E. V. Dmitrieva, F. F. Murzakhanov, et al., "Probing Remote Nuclear Magnetic Moments in hBN with VB^- Electron Spin," *Applied Physics Letters* 127, no. 2 (2025): 024001, https://doi.org/10.1063/5.0280411.

42. E. Janzen, H. Schutte, J. Plo, et al., "Boron and Nitrogen Isotope Effects on Hexagonal Boron Nitride Properties, *Advanced Materials* "36, no. 2 (2023): 2306033, https://doi.org/10.1002/adma.202306033.

43. J. R. Reimers, J. Shen, M. Kianinia, et al., "Photoluminescence, Photophysics, and Photochemistry of the VB^- Defect in Hexagonal Boron Nitride," *Physical Review B* 102, no. 14 (2020): 144105, https://doi.org/10.1103/PhysRevB.102.144105.

44. C. Cholsuk, T. Vogl, and V. Ivády, "Spin Relaxation Mechanisms and Nuclear Spin Entanglement of the V_B^{-1} Center in hBN," *npj Computational Materials* 11, no. 1 (2025): 344, https://doi.org/10.1038/s41524-025-01859-0.

45. L. J. Rogers, R. McMurtrie, M. Sellars, and N. B. Manson, "Time-Averaging within the Excited State of the Nitrogen-Vacancy Centre in Diamond," *New Journal of Physics* 11, no. 1 (2009): 063007, https://iopscience.iop.org/article/10.1088/1367-2630/11/6/063007.

46. A. Durand, T. Clua-Provost, F. Fabre, et al., "Optically Active Spin Defects in Few-Layer Thick Hexagonal Boron Nitride," *Physical Review Letters* 131, no. 11 (2023): 116902, https://doi.org/10.1103/PhysRevLett.131.116902.

47. J. Li, C. Elias, G. Ye, et al., "Single Crystal Growth of Monoisotopic Hexagonal Boron Nitride from a Fe-Cr Flux," *Journal of Materials Chemistry C* 8, no. 29 (2020): 9931–9935, https://doi.org/10.1039/D0TC02143A.

48. S. Liu, R. He, L. Xue, J. Li, B. Liu, and J. H. Edgar, "Single Crystal Growth of Millimeter-Sized Monoisotopic Hexagonal Boron Nitride," *Chemistry of Materials*, 30, no. 18, (2018): 6222–6225, https://doi.org/10.1021/acs.chemmater.8b02589.

Supporting Information

Additional supporting information can be found online in the Supporting Information section.

Supporting File: adfm73890-sup-0001-SuppMat.pdf.